Chemical Engineering Journal 375 (2019) 121998

Contents lists available at ScienceDirect

Chemical Engineering Journal

journal homepage: www.elsevier.com/locate/cej

Carbon coated transition metal borates as anode materials for Na-ion batteries

Kaiqiang Zhou[a,1], Guigui Xu[b,1], Yang Chen[a], Zhiqing Chen[a], Jinxian Huang[a], Yichao Zhen[a], Zhigao Huang[a,c], Zhensheng Hong[a,c,*]

[a] Fujian Provincial Key Laboratory of Quantum Manipulation and New Energy Materials, College of Physics and Energy, Fujian Normal University, Fuzhou, Fujian 350117, China

[b] Concord University College Fujian Normal University, Fuzhou 350117, China

[c] Fujian Provincial Collaborative Innovation Center for Optoelectronic Semiconductors and Efficient Devices, Xiamen 361005, China

HIGHLIGHTS

- Two transition metal borates are proposed as new promising anode materials for NIBs.
- The conversion reaction can be thoroughly realized for transition metal borates.
- Na insertion into transition metal borates are energetically more favorable than oxides.
- $Fe_3BO_5/Na_2V_3(PO_4)_2F_3$ full cell exhibits a high energy density of 180.3 Whkg^{-1}.

ARTICLE INFO

Keywords:
Transition metal borates
Conversion-type anode
Na-ion batteries
Carbon coating

ABSTRACT

Development of anode materials with high performance is crucial for the successful application of Na-ion batteries. In this study, we provide a novel type of conversion-type anode materials, transition metal borates, as promising candidates for Na-ion storage. The transition metal borates (Fe_3BO_5 and $Ni_3(BO_3)_2$) are successfully fabricated by a facile sol-gel route. When they are firstly evaluated for Na-ion storage, they deliver remarkably better Na-ion insertion kinetics and high reversible capacity than transition metal oxides. It's notable that the conversion reaction can be thoroughly realized for transition metal borates during sodiation/desodiation process accompanying with the change of B-O coordination. First-principles calculation indicates that Na insertion into transition metal borate are energetically much more favorable compared with transition metal oxides. Furthermore, carbon coated borates are designed and firstly prepared, which exhibit good rate capability and excellent cycling stability. Moreover, the $Fe_3BO_5/Na_2V_3(PO_4)_2F_3$ full cell exhibits a high energy density of 180.3 Wh kg^{-1} at a high power density of 150.1 W kg^{-1}. This study demonstrates a class of new promising conversion-type anodes and also verifies the practical application in Na-ion batteries with high energy/power density.

1. Introduction

Electrical energy storage (EES) is a significant technology for the conversion and storage of green energy resources [1]. Lithium ion batteries (LIBs), which are lightweight and possess an available capacity ranging from 700 to 2500 mAh for a small cell, are widely applied in power portable electronic devices [2,3]. However, lithium resources are scarce, pocket and high cost, which prohibit large-scale application of LIBs. Thus, it is indispensable to exploit alternative EES device to replace LIBs. When Na-ion batteries (NIBs) emerge into our sight again, it rapidly attract much attentions due to the abundant sodium resources, similar metal ions storage mechanism to LIBs and acceptable energy density [4–6]. As the electrode material is an important content of LIBs, it is also a vital part of NIBs, particularly anode material [7]. Up to now, there are plentiful materials that have been found and applied as anode materials for NIBs [8–11]. These contain carbon-based

* Corresponding author at: Fujian Provincial Key Laboratory of Quantum Manipulation and New Energy Materials, College of Physics and Energy, Fujian Normal University, Fuzhou, Fujian 350117, China.
E-mail address: winter0514@163.com (Z. Hong).

[1] These authors contributed equally to this work.

https://doi.org/10.1016/j.cej.2019.121998
Received 4 March 2019; Received in revised form 15 May 2019; Accepted 16 June 2019
Available online 17 June 2019
1385-8947/

materials (typically for hard carbon) [12], transition metal oxides (Fe_2O_3, TiO_2, etc.) [13,14], transition metal sulfides (CoS, NiS, SnS, etc.) [15–17] and alloy-based materials (Sn, Bi, P, etc.) [18,19]. Among these anode materials, transition metal oxides were chosen as suitable anode material owing to their abundances and high theoretical capacity based on conversion-type storage mechanism [11,20]. However, there have been some common obstacles for transition metal oxides. One of the obstacles is the large volume changes during Na^+ ion insertion/extraction, leading to agglomeration or pulverization as well as fast capacity weakening. The other obstacle is the low initial Coulombic efficiency probably arising from its low electronic and ionic conductivity [21,22]. With many efforts contributed by researchers, various strategies have been carried out to solve these problems. Designing and fabricating nonstructural materials and metal oxide/carbon-based composites (M_xO_y/graphene, carbon coated M_xO_y, M_xO_y/carbon nanotubes) were widely investigated [23–28]. Although these studies provide some valuable strategies to resolve the decay of conversion-type anode, the complicated and laborious synthesis routes render them far from real application.

In 1997, the borates were mentioned firstly by Idota et al. as alternative for anode materials in LIBs [29]. The distinction between transition metal borates and transition metal oxides is the introduction of boron element in the structure. The boron element has a low atomic weight, causing the higher specific capacity of the borates [30,31]. What's more, the boron can form a series of clusters (such as BO_3^{3-}, BO_4^{5-} and BO_6^{9-}) with oxygen atom, which has many electronegativity sites to bond the cations and make the borates turn into various structure. These characteristics can reduce the voltage polarization [32] and offer various redox potentials when they are adjacent to cations [33–36]. Accordingly, various transition metal borates ($Ni_3B_2O_6$, $Co_3B_2O_6$ and $Cu_3B_2O_6$) were proposed and demonstrated promising application in LIBs [7,37–40]. In consideration of the similar mechanism between NIBs and LIBs, transition metal borates could be a class of promising anode materials of NIBs as well. In 2017, Fe_3BO_6 was firstly studied as anode of NIBs, and showed satisfied reversible Na-ion storage capacity after carbon coating based on the similar conversion-type storage mechanism to Li-ion storage [36]. However, the report about transition metal borates for Na-ion storage performance is rare until now and their potential applications in NIBs needs to be explored [41].

Herein, we focus on the comparative investigation of transition metal borates and transition metal oxides as potential anodes for NIBs. Firstly, two kinds of transition metal borates (Fe_3BO_5 and $Ni_3(BO_3)_2$) were successfully prepared through sol-gel method. Then, the Na-ion storage performance of such transition metal borates were firstly investigated, demonstrating remarkably larger reversible capacity compared with transition metal oxides (Fe_3O_4 and NiO). Theoretical calculation revealed that it requires much lower energy when Na-ion insert into borates compared with oxides. Furthermore, carbon coated borates (Fe_3BO_5@C and $Ni_3(BO_3)_2$@C) was obtained to improve the rate capability and cycling performance. It is also revealed only a part of transition metal oxide can be transformed, while conversion reaction can be thoroughly achieved for transition metal borates during the sodiation/desodiation. This finding is significantly meaningful for the design of conversion-type anodes and their practical application in NIBs.

2. Experimental

2.1. Materials synthesis

Carbon coated Fe_3BO_5 (Fe_3BO_5@C) was fabricated by the reduction of Fe_3BO_6. Firstly, Fe_3BO_6 was synthesized through a sol-gel method. 1.01 g iron(III) nitrate nonahydrate ($Fe(NO_3)_3{\cdot}9H_2O$) and 0.465 g boracic acid (H_3BO_3) were successively dissolved in 50 mL deionized water under stirring. And then, 1.31 g citric acid was added into the solution as chelating agent. After stirring for half an hour, this solution was put into blast air oven and kept at 150 °C for 10 h. Sequentially, the brown powders were collected in alumina crucible and annealed at 750 °C for 4 h. Finally, the Fe_3BO_6 was obtained. Subsequently, Fe_3BO_6 were milled with 500 rpm rotate speed for 12 h. After that, 200 mg Fe_3BO_6 was ultrasonic dispersed into a Tris-buffer solution (100 mL, 10 mM) for 1 h. And then, 100 mg dopamine was added into the solution, followed by stirring for 10 h. The black product (Fe_3BO_6@PDA) was collected and washed several times with deionized water and ethanol and dried at 60 °C. Finally, Fe_3BO_5@C was obtained by annealing Fe_3BO_6@PDA precursor at 600 for 2 h under Ar atmosphere. In addition, $Ni_3B_2O_6$ and carbon coated $Ni_3(BO_3)_2$ ($Ni_3(BO_3)_2$@C) were obtained through the same process as the Fe_3BO_6 and Fe_3BO_5@C, instead of the use of Nickel (II) acetate tetrahydrate ($Ni(CH_3COO)_2{\cdot}4H_2O$). In addition, 0.1 M HCl solution was used to dissolve the nickel metal in $Ni_3(BO_3)_2$@C coming from its part reduction during carbonization. Fe_3O_4@C and NiO were synthesized following the above process without the H_3BO_3.

2.2. Electrochemical measurements

To test the storage performance of Na-ion for these materials, the working electrodes, containing active materials, were made through a common slurry-coating process. Typically, the active material was admixed with super-P (SCM Industrial Chemical Co.Ltd.) and arabic gum (Sigma) in a weight ratio of 80:10:10. Then, this slurry was coated on the copper foil as working electrode and dried at 120 °C in vacuum overnight. Subsequently, this foil was tailored to a 12.5 mm diameter disc with a loading density of around 1.0 $mgcm^{-2}$. NIBs were fabricated in coin cell (CR2025) in a glove box which was filled with argon gas (O_2 and H_2O levels < 1 ppm) and a Na metal foil as the counter electrode, glass fiber separator (Whatman GF/F) and 1 M $NaPF_6$ in Diethylene glycol dimethyl ether as the electrolyte. The capacity ratio between cathode and anode of the full cell is ~1.1 (anode/cathode). The galvanostatic charge/discharge tests of the cells were performed with a multichannel battery testing system (Wuhan, LAND, China). Cyclic voltammograms (CV) measurements at a scanning rate of 0.5 mVS^{-1} were conducted on Zennium (Zahner).

3. Results and discussion

The core-shell structure Fe_3BO_5@C and Fe_3O_4@C were synthesized through the reduction of Fe_3BO_6 and Fe_2O_3, which were fabricated by sol-gel route and then coated with PDA. The structure and morphology of Fe_3BO_6 and Fe_2O_3 are identified by X-ray diffraction (XRD) patterns and SEM images, as shown in Fig. S1. Fig. 1a shows the XRD patterns of the as-prepared samples. XRD diffraction peaks of Fe_3BO_5@C and Fe_3O_4@C can be precisely associated with orthorhombic vonsenite $Fe_2Fe(BO_3)O_2$ (JCPDS 25-0395) and cubic Fe_3O_4 (JCPDS 26-1136), respectively. The diffraction peaks of both samples are very sharp, suggesting high crystallization due to the high annealing temperature. The SEM images of Fe_3BO_5@C and Fe_3O_4@C are displayed in Fig. 1b and c. The size of two samples are mostly around 40–100 nm. It's notable that a core-shell structure is clearly presented for the two samples. TEM image of Fe_3BO_5@C (Fig. 1d) further confirm this morphology. Fe_3BO_5 nanoparticles were uniformly coated by a carbon shell. In addition, the HAADF-STEM image and elemental mapping were also used for further investigating the structure of the composites. As shown in Fig. 1e–h, a core-shell structure with uniform carbon layer is observed for Fe_3BO_5@C. The contents of the carbon shell is 4.3% calculating from the thermogravimetric analysis (Fig. S2a) and the Raman spectrum (Fig. S2c) indicates that there are two obvious peaks at ~1340 (D-band) and ~1590 cm^{-1} (G-band), which correspond to the vibrations of carbon structure. It also suggests the presence of some disoriented or defect structure in such nanocarbon materials. In the previous reports, the same result was also found that core-shell structure is formed after the reduction of Fe^{3+} (Fe_2O_3) to Fe^{2+} (Fe_3O_4), resulting in the grain

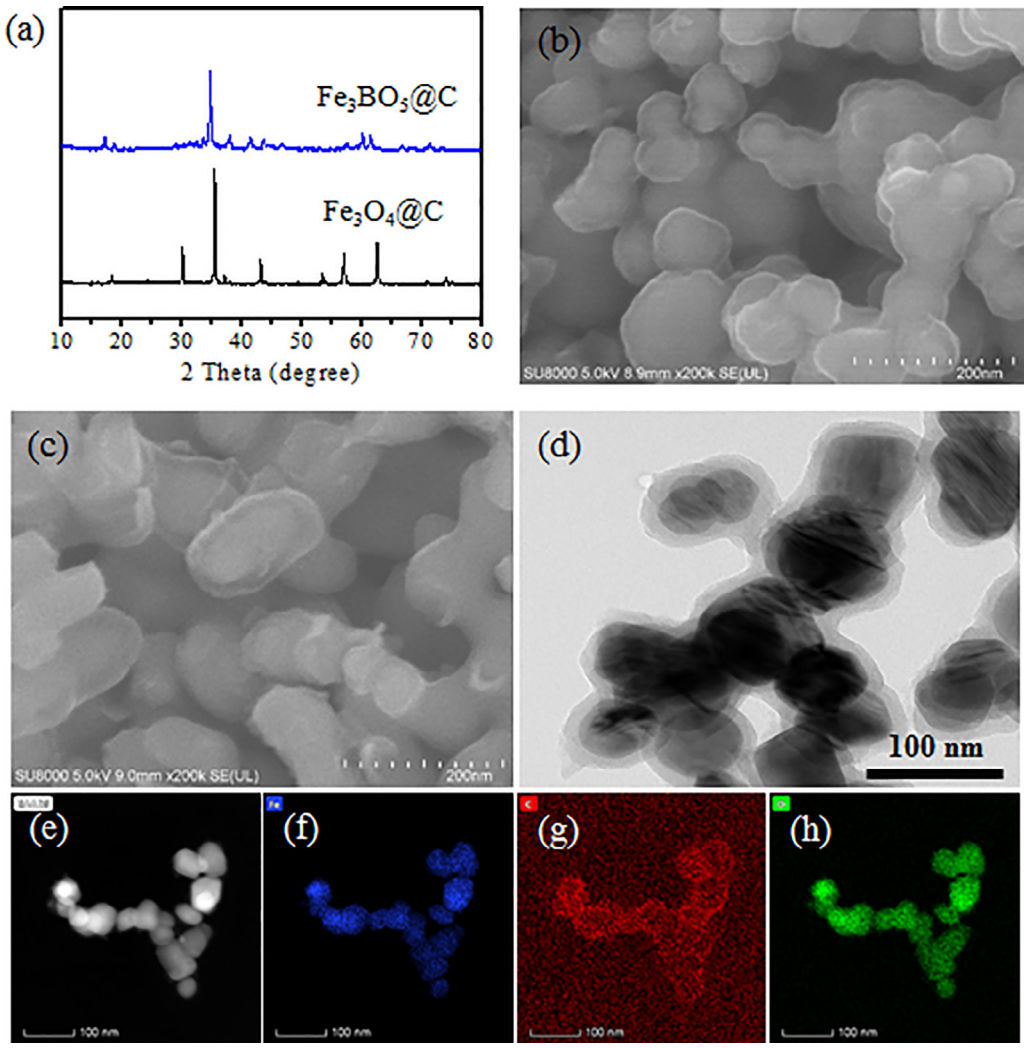

Fig. 1. (a) XRD patterns of Fe_3BO_5@C and Fe_3O_4@C. SEM images of (b) Fe_3BO_5@C and (c) Fe_3O_4@C. (d) TEM image of Fe_3BO_5@C. (e) HAADF-STEM image and elemental mapping of (f) Fe, (g) C and (h) O from Fe_3BO_5@C.

shrinking during the carbonization process of PDA [42]. However, core-shell structure Fe_3BO_5@C was firstly achieved in this study, which may possess expected electrochemical performance.

Accordingly, $Ni_3(BO_3)_2$ (NiBO) and NiO nanomaterials were synthesized by the sol-gel method and NiBO@C was prepared through the same route. The verification of crystalline phase and the microstructure of these materials can be found from Fig. 2. From the XRD patterns displayed in Fig. 2a, it's concluded pure phase orthorhombic $Ni_3(BO_3)_2$ (JCPDS 26-1284) and cubic NiO (JCPDS 47-1049) were successfully prepared. From the SEM images (Fig. 2b–e), close-packed grain is observed for NiO with size from 20 nm to 60 nm. NiBO shows nanorod morphology with diameter about 60–100 nm. It should be mentioned that NiBO@C was also coated by a uniform carbon layer with carbon content is 2.4% coming from the thermogravimetric analysis. The presence and structure of carbon is identified by Raman spectrum (Fig. S2d). Such a well coating carbon layer can be found from TEM image (Fig. 2f). Furthermore, HAADF-STEM image and elemental mapping for NiBO@C (Fig. 2g–j) also confirm a uniform carbon coating. In addition, the size of NiBO decreased to a certain extent after carbon coating due to the reduction reaction with carbon. The pure NiBO@C sample can be obtained after removing the produced metal Ni by diluted HCl solution. In a word, these results demonstrated a general method for the synthesis of uniform carbon coated transition metal borates.

Up to now, it is scarce to study the Na-ion storage performance of transition metal borates as well as the relationship between their structure and properties. In this work, the comparative investigation of transition metal borates and transition metal oxides for Na-ion storage was evaluated by Na-ion half cells. The first five CV curves of Fe_3BO_5@C and Fe_3O_4@C electrodes were performed between 0.01 and 3 V with a scan rate of 0.5 mVS^{-1}, shown in Fig. 3a and b. An obvious cathodic peak at 0.3 V at the first cycle can be largely attributed to the reduction of Fe^{3+}/Fe^{2+} to metal Fe accompanying with the generation of the solid electrolyte interphase (SEI) film. A broad anodic peak around 1.3 V is observed at the anodic curve, which corresponds to the oxidation of the metallic iron to iron oxide (Fe^{2+}) [43]. In the subsequent CV curves, they exhibit high reproducibility with cathodic peaks at 0.7 V and the anodic peaks at 1.3 V, demonstrating good cycling performance of Fe_3BO_5@C electrode [36]. As a comparison, the CV peak intensity of Fe_3O_4@C (Fig. 3b) is weak and much lower than that of Fe_3BO_5@C electrode, suggesting poor electrochemical activity. The cathodic peaks at 0.37 V was also arising from the reduction of Fe_3O_4 to metal Fe at the first cycle. Meanwhile, two anodic peaks at 1.91 and 2.1 V can be attributed to the oxidation of metal Fe [44–46]. It can be noticed that the cathodic peaks at 0.37 V still occurred at the following curves, indicating that the conversion reaction continually proceed. This result further confirms the low electrochemical activity and conversion rate of Fe_3O_4@C electrode for SIBs.

Fig. 3c and d present the charge-discharge profiles of Fe_3BO_5@C and Fe_3O_4@C electrodes at 50 mAg^{-1}. Fe_3BO_5@C displays a large discharge capacity of 653.5 $mAhg^{-1}$ and charge capacity of

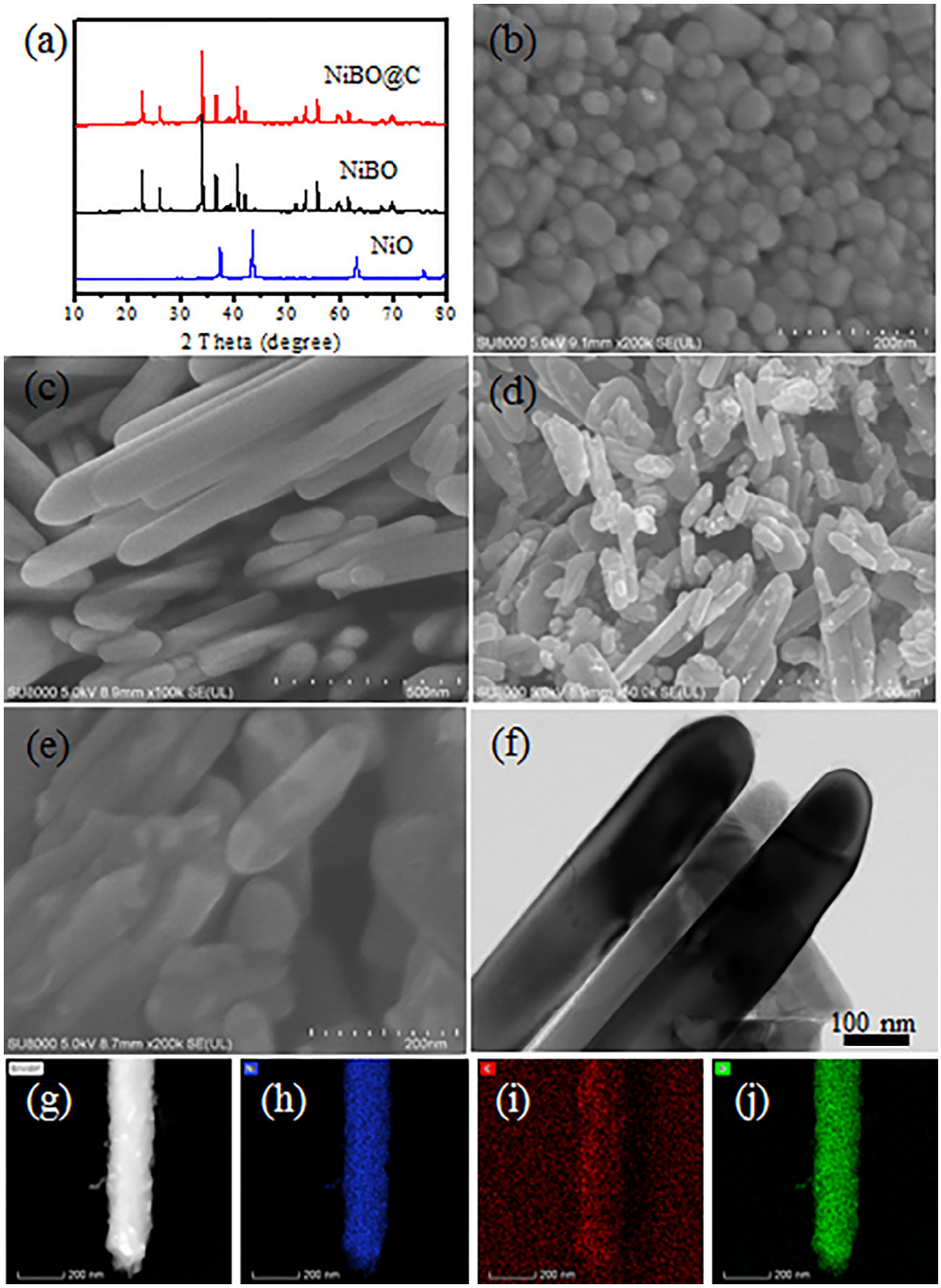

Fig. 2. (a) XRD patterns of NiO, NiBO and NiBO@C. SEM images of (b) NiO, (c) NiBO and (d, e) NiBO@C. (f) TEM image of NiBO@C. (g) HAADF-STEM image and elemental mapping of (h) Fe, (i) C and (j) O from NiBO@C.

471.9 mAhg^{-1} at the first cycle, while Fe_3O_4@C only displays a limit discharge capacity of 141.1 mAhg^{-1} (107.8 mAhg^{-1} for charge). An obvious discharge plateaus located around 0.5 V can be clearly observed for Fe_3BO_5@C, representing the proceeding of conversion reaction of the electrode material. However, this is barely visible for Fe_3O_4@C. This remarkable difference demonstrates that iron borate exhibits significantly higher Na-ion storage activity than ferriferrous oxide. The rate capability of the samples was further evaluated from 50 to 2000 mAg^{-1}. Fe_3BO_5@C exhibits a reversible charge capacity of ~470 mAhg^{-1} at 50 mAg^{-1} (~107 mAhg^{-1} for Fe_3O_4@C) and ~142 mAhg^{-1} (~41 mAhg^{-1} for Fe_3O_4@C) at a relatively high rate of 2000 mAg^{-1}. When the rate returned to 100 mAg^{-1}, it gets back a high reversible capacity of ~420 mAhg^{-1}. Because of the superior rate performance of Fe_3BO_5@C, the cycling performance and Coulomb efficiency (Fig. 3f) are also investigated at constant current density of 100 mAg^{-1}, which displays excellent stability with retaining capacity around 400 mAhg^{-1} after 350 cycles and high Coulomb efficiency around 100% during cycling.

The sodium storage properties of nickel borate and nickel oxide were also studied, as shown in Fig. 4. NiBO@C electrode shows a significant cathodic peak around 0.3 V at the first cycle (Fig. 4a), which can be ascribed to the reduction of Ni^{2+}. In addition, the pure NiBO electrode exhibits the similar CV curves (Fig. S3a). Although NiO electrode shows a similar cathodic peak around 0.2 V at the first CV scan (Fig. 4b), the redox peak current is quite small compared with nickel borate. Thus, the nickel borate exhibits remarkably higher Na-

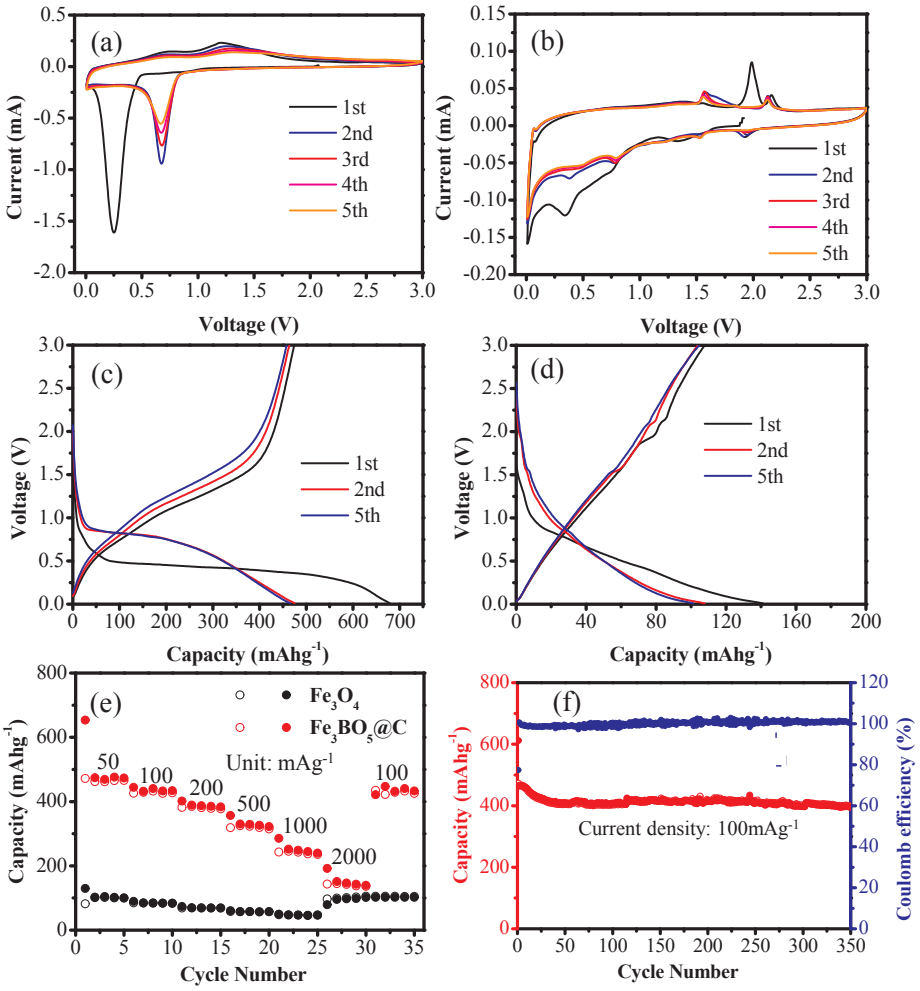

Fig. 3. CV curves of (a) Fe_3BO_5@C and (b) Fe_3O_4@C at a scan rate of 0.5 mVs^{-1} in the voltage range of 0.01–3 V. Galvanostatic discharge and charge profiles for the 1st, 2nd and 5th cycles of (c) Fe_3BO_5@C and (d) Fe_3O_4@C at a current density of 50 mAg^{-1}. (e) Rate capability of Fe_3BO_5@C and Fe_3O_4@C at the current density range from 50 to 2000 mAg^{-1}. (f) Cycling performance and Coulombic efficiency of Fe_3BO_5@C at a current density of 100 mAg^{-1}.

ion insertion kinetics than nickel oxide even with a larger size. Discharge and charge profiles of these samples are presented in Fig. 4c, d. NiBO@C exhibits remarkably higher capacity (755 $mAhg^{-1}$) than that of NiO (138.4 $mAhg^{-1}$) at the first discharge. The distinct platform around 0.5 V of NiBO@C and NiBO (Fig. S3b) are also apparent, which is not found for NiO. What's more, NiBO@C delivers much higher reversible capacity (619 $mAhg^{-1}$) than NiO (104 $mAhg^{-1}$). This result suggests that the conversion reaction between nickel borate and metal nickel is completely achieved and reversible. The rate capability and cycling stability of NiO, NiBO and NiBO@C were investigated, as displayed in Fig. 4e. NiBO@C exhibits more outstanding rate performance (~240 $mAhg^{-1}$ at 2000 mAg^{-1}) and cycling stability (~420 $mAhg^{-1}$ after 150 cycles at 100 mAg^{-1}) than the other two samples. Meanwhile, the high coulomb efficiency around 100% is also presented in Fig. 4e. It should be pointed out that NiBO electrode without carbon coating has poor cycling performance largely owing to the large volume expansion of conversion type electrode. The storage capacity of NiO is very limited due to the poor Na-ion insertion activity. These results reveal that transition metal borates possess remarkably higher Na-ion insertion activity and better sodium storage properties than transition metal oxides.

For the sake of revealing the sodium storage mechanism, NiO and NiBO electrodes at different discharge and charge states were opened up in glove box with argon gas atmosphere, and the corresponding XRD patterns of these electrodes are shown in Fig. 5a, b. In Fig. 5a, the diffraction peaks of NiBO phase were disappeared instead of the presence of metallic nickel at 44.5° after the first sodiation process (as highlighted in the inset). And NiO can be found based on the diffraction peaks 44.3° of NiO after the first desodiation. As a contrast, the XRD patterns of NiO electrode at different working states are presented in Fig. 5b. It should be noticed that NiO is the main content in the electrode and were always existent during the first cycles, and a small content of metallic nickel can be found after first sodiation. Thus, the complete conversion reaction for nickel borate can be realized, but only a few NiO participated in the electrode reaction. This result well explains why nickel borate exhibits high sodium storage capacity and nickel oxide has low capacity. Meanwhile, the XRD patterns of Fe_3BO_5@C and Fe_3O_4@C are shown in Fig. S4a, b. It is obvious that it demonstrates the similar results as NiBO and NiO. Fe_3BO_5 can be converted to metal Fe at the first discharge process, and it can be transformed to FeO after the charge process. However, Fe_3O_4 were always existent at different working states and the other phase was almost not found. In other words, it can be concluded that the introduction of the boron is greatly in favor of the conversion reaction of transition metal cations, leading to large sodium storage capacity.

Furthermore, the Fourier Transform infrared spectroscopy (FT-IR) were carried out to investigate the change of structure of borate during sodiation/desodiation (Fig. 5c). All of the electrodes have two peaks at 621 cm^{-1} and 691 cm^{-1}, which are well coincident to the bending mode of B-O. The peaks at 1185 cm^{-1}, 1236 cm^{-1} and 1409 cm^{-1} can be ascribed to B-O stretching of trigonal BO_3 units for the fresh electrode [33,39]. The peaks at 1340 and 1570 cm^{-1} are largely due to B-O

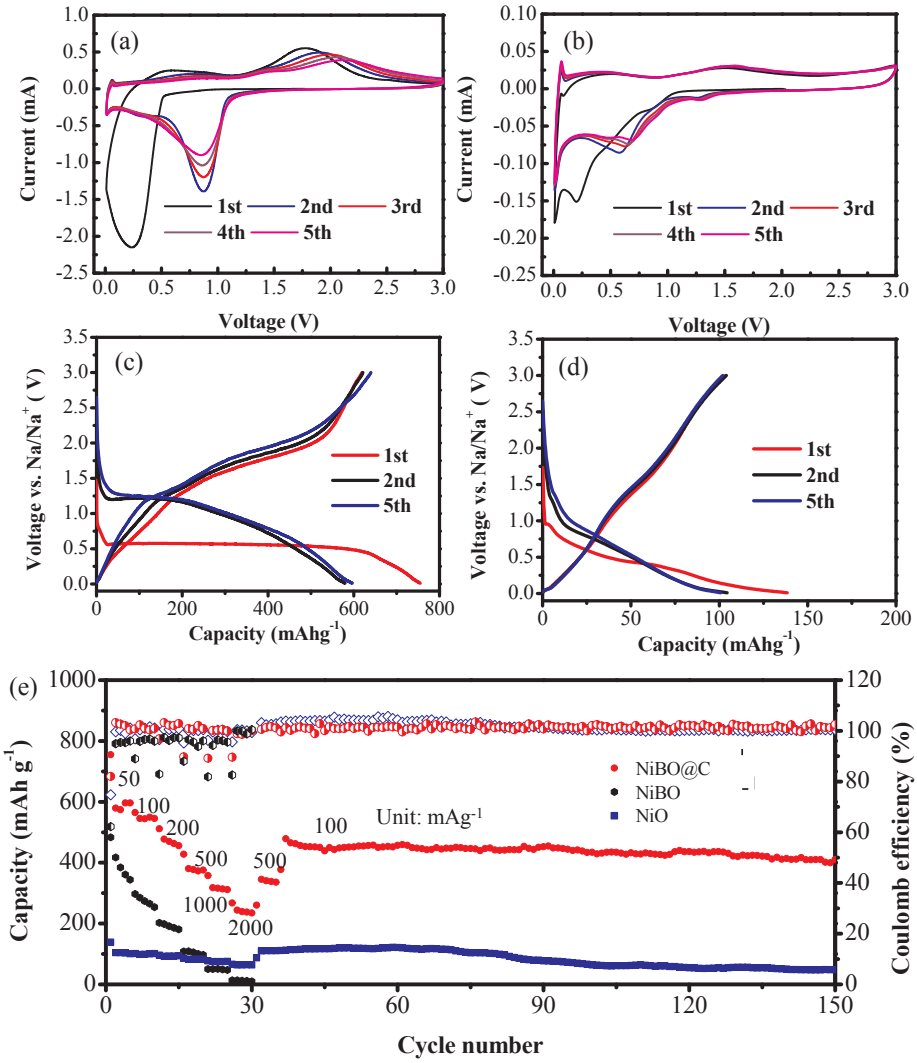

Fig. 4. CV curves of (a) NiBO@C, and (b) NiO at 0.5 mV s^{-1} in the voltage range of 0.01–3 V. The discharge and charge profiles for the1st, 2nd and 5th cycles of (c) NiBO@C and (d) NiO at a current density of 50 mAg^{-1}. (e) Rate capability and cycling stability and Coulombic efficiency of NiO, NiBO and NiBO@C.

asymmetric stretching of trigonal BO_3 units for the electrodes after the first discharge and charge [47]. These two blue shift peaks may be due to the broken of Ni-O-B and the formation of Na-O-B [48]. It should be noted that the new emergent peaks at 996 cm^{-1} and 837 cm^{-1} at the discharge state can be ascribed to the B-O asymmetric and symmetric stretching of tetrahedral BO_4 units, respectively. These two peaks became weak and the peak 1570 cm^{-1} belong to trigonal BO_3 units strengthened at the charge state. Therefore, it is deduced that the structure of the borate was transformed between trigonal BO_3 units and tetrahedral BO_4 units during sodiation/desodiation process. Meanwhile, X-ray photoelectron spectroscopy (XPS) further uncovers the chemical structure of the NiBO electrodes. The full XPS spectrum is displayed in Fig. S5a. As shown in Fig. 5d, the peak of B 1 s at 191.8 eV corresponding to the binding energy of the borates divided into three peaks located at 194.0, 192.0 and 190.2 eV after the discharge, demonstrating the presence of $Na_2B_4O_7$ and/or other sodium borates ($Na_3B_3O_6$) [49]. After achieving the charge process, only one peak at 192.0 eV is existent, which reveals that the conversion of $Na_2B_4O_7$ during Na-ion storage process. The peaks of Ni $2p_{2/3}$ spectrum (Fig. 5e) at 854.3 and 860.5 eV for the fresh electrode are shifted to low binding energy at 853.8 eV and 859 eV after discharge, which verifies the reduction reaction of Ni^{2+} to metal Ni during sodiation process. In addition, the peaks at 850.1 and 861.2 eV verify the recurrence of Ni^{2+} after desodiation process [50]. For the O 1 s spectrum as shown in Fig. 6f, the peak at ~532.5 eV and 530.8 eV for the fresh electrode can be ascribed to B-O bond and Ni-O eV. The Na-O peak at 531.2 eV is found after the discharge, but it was reduced after charge [51]. This suggests the extraction of Na from sodium borates, corresponding to the above XPS results of B element. Besides, the Na 1 s located at 1071.8 eV (Fig. S5b) can be clearly observed after first sodiation process which is not found in fresh electrode. Therefore, the XPS result further confirms the conversion reaction of nickel borate electrode to metal Ni and sodium borate, accompanying with the change of B-O coordination during sodiation/desodiation process.

According to the careful structure characterization of NiBO@C during discharge and charge process, the discharge process equation can be provided as follow:

$$3Ni_3(BO_3)_2 + 18Na^+ + 18e^- \rightarrow 9Ni + 9Na_2O{\cdot}3B_2O_3$$

And the charge process equation can be described as follow:

$$Ni + 9Na_2O{\cdot}3B_2O_3 \rightarrow NiO + 2Na^+ + 8Na_2O{\cdot}3B_2O_3 + 2e^-$$

The phase transition of the sodium borates between $9Na_2O{\cdot}B_2O_3$ and $8Na_2O{\cdot}B_2O_3$ can be revealed from FTIR and XPS. It should be noted that $9Na_2O{\cdot}B_2O_3$ represent the structure of sodium borate including $B_4O_7^{2-}$ group and the composites of BO_3^{3-} and BO_4^{5-} groups, where $8Na_2O{\cdot}B_2O_3$ represent BO_3^{3-} and BO_4^{5-} groups [41]. The electrochemical reaction of Fe_3BO_5@C is similar to NiBO@C. Therefore, the

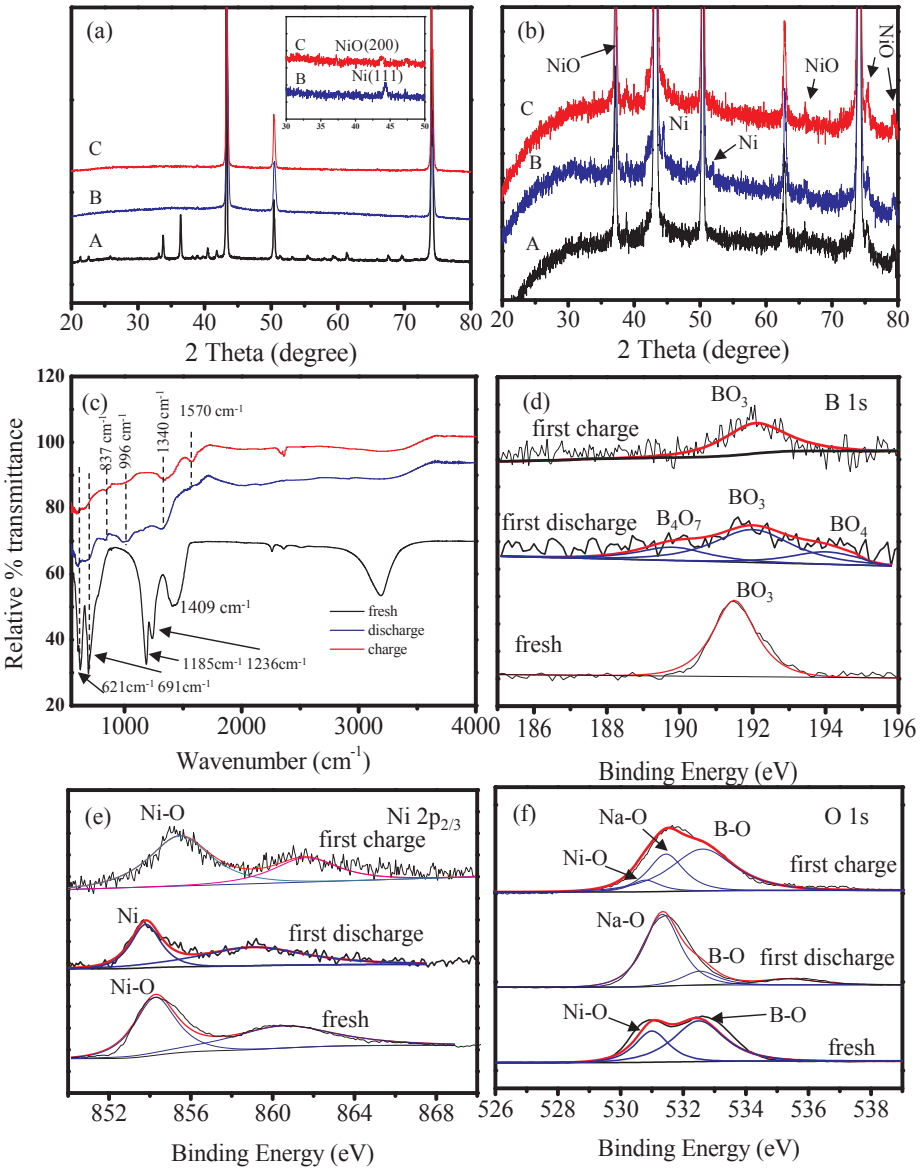

Fig. 5. XRD patterns of (a) NiBO and (b) NiO electrodes at different working states: fresh electrode (curve A), first discharge (curve B) and first charge (curve C), inset is the enlarged pattern of NiBO. (c) FTIR patterns of NiBO electrodes. XPS spectrum of NiBO electrodes spectrum, (e) Ni $2p_{2/3}$ spectrum and (f) O 1 s spectrum.

discharge process equation can be deduced as follow:

$$2Fe_3BO_5 + 14Na^+ + 14e^- \rightarrow 6Fe + 7Na_2O\cdot B_2O_3$$

Accordingly, the theoretical capacity of Fe_3BO_5 and $Ni_3(BO_3)_2$ can be up to 547.3 $mAhg^{-1}$ and 726.8 $mAhg^{-1}$, respectively.

To further compare the energetic and thermal stability of the sodium insertion reactions, we define and calculate their formation energies through first-principle methods. The sodium insertion reaction for transition metal oxide (MO, M = Ni, Fe) and transition metal borate (MBO, M = Ni, Fe) can be expressed by

$$M_xO + (x-y)Na \rightarrow M_yNa_{x-y}O + (x-y)M \quad (1)$$

$$M_xBO + (x-y)Na \rightarrow M_yNa_{x-y}BO + (x-y)M \quad (2)$$

The corresponding formation energies for Na inserted into M sites in MO and MBO are defined as follows [52,53]:

$$E_f = \frac{E(M_yNa_{x-y}O) + (x-y)E(M) - E(M_xO) - (x-y)E(Na)}{x-y} \quad (3)$$

$$E_f = \frac{E(M_yNa_{x-y}BO) + (x-y)E(M) - E(M_xBO) - (x-y)E(Na)}{x-y} \quad (4)$$

where $E(M_yNa_{x-y}O)$, $E(M_xO)$, $E(M_yNa_{x-y}BO)$, $E(M_xBO)$, $E(M)$, and $E(Na)$ are the calculated total energies of $M_yNa_{x-y}O$, M_xO, $M_yNa_{x-y}BO$, M_xBO, transition metal M (M = Ni, Fe), and Na metal, respectively.

Fig. 6a and b presents the calculations models for $Ni_3(BO_3)_2$ (NiBO) and NiO, respectively. In NiBO, Ni ions occupy two different Ni sites [Ni (1) and Ni(2) site shown in Fig. 6a. Therefore, there are two types of Na insertion into Ni sites in NiBO, denoted as Na/Ni(1) and Na/Ni(2), respectively. In the case of NiO, all the Ni ions occupy the same Ni sites as shown in Fig. 6b. Table S1 summarizes the calculated formation energies for Na inserted into Ni sites in NiBO and NiO. It should be significantly notable from Table S1 that the formation energies (minimum value of −2.21 eV) of the Na insertion into Ni sites in NiBO are much lower than that in NiO (−1.681 eV). This implies that Na insertion into NiBO is energetically more favorable. Fig. 6c and d show the structures for Fe_3BO_5 and Fe_3O_4, respectively. The calculated formation energies of Na insertion into Fe sites in Fe_3BO_5 and Fe_3O_4 are listed in Table S2.

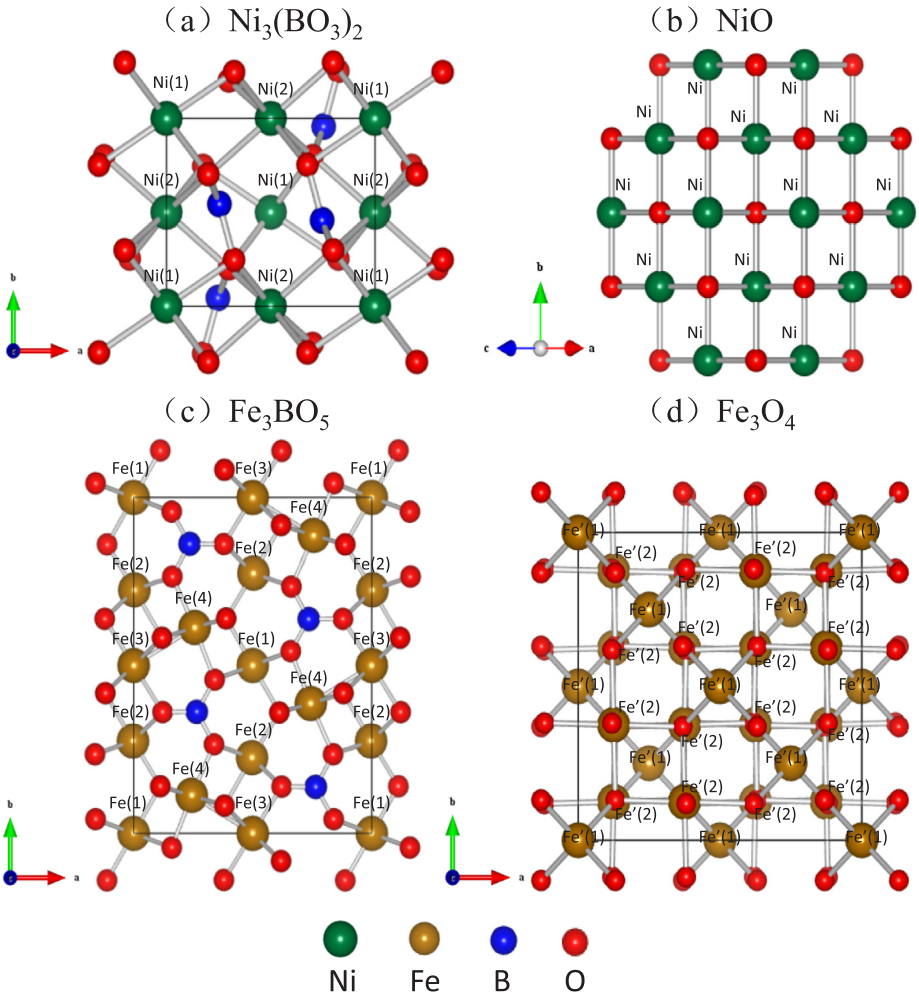

Fig. 6. Unit-cell structures of (a) $Ni_3(BO_3)_2$, (b) NiO, (c) Fe_3BO_5, and (d) Fe_3O_4. The dark green, brown, blue, and red balls represent Ni, Fe, B, and O, respectively. Different types of Ni sites and Fe sites in various structures are labeled.

It is also clear to find that the formation energies (minimum value of −2.59 eV) of the Na insertion into various Fe sites in Fe_3BO_5 [Fe(1), Fe (2), Fe(3), and Fe(4) site in Fig. 6c] are all lower than those in Fe_3O_4 (minimum value of −2.1 eV), indicating that Na prefers to insert into Fe_3BO_5 compared to Fe_3O_4. Based on the above calculated results, we can conclude that Na insertion into transition metal borate (e.g., $Ni_3(BO_3)_2$ and Fe_3BO_5) are energetically much more favorable relative to transition metal oxide (e.g., NiO and Fe_3O_4). These results agree well with the experimental findings in this work.

In order to further test the practical application of the borates on the energy storage device, Fe_3BO_5 anode were assembled with $Na_2V_3(PO_4)_2F_3$ cathode to constitute a $Fe_3BO_5/Na_2V_3(PO_4)_2F_3$ full cell. The cathode material was prepared through the previous literature [54]. The electrochemical performances of $Na_2V_3(PO_4)_2F_3$ cathode is shown in Fig. S6, delivering good rate capability and cycling stability. The charge and discharge profiles of $Fe_3BO_5/Na_2V_3(PO_4)_2F_3$ full cell is presented in Fig. 7a, which demonstrating a high working voltage compared with the-state-of-art Na-ion full batteries [41]. In addition, the capacity of the cathode side is used to illustrate the full cell capacity). Fig. 7b shows the rate performance of $Fe_3BO_5/Na_2V_3(PO_4)_2F_3$ full cell at different current density and exhibits average discharge capacities of ~90.4, ~76.7 ~62.0, ~48.7, and ~38.2 $mAhg^{-1}$ at 100, 200, 500, 1000 and 2000 mAg^{-1}. Accordingly, the energy density of the full cell is 180.30 $Whkg^{-1}$ and the power density is 150.1 Wkg^{-1} (calculating on the basis of total mass of anode and cathode). Fig. 7c presents the cyclic performance for the full cell at the current density of 200 mAg^{-1} and a stable capacity of 72.9 $mAhg^{-1}$ can be remained after 100 cycles, which demonstrates good cycling stability of the device. Therefore, the borates can be applied in practical energy storage devices with good performance and low cost.

4. Conclusion

In conclusion, the comparative study of transition metal borates and transition metal oxides as potential conversion-type anodes for NIBs is firstly achieved in this study. Two kinds of transition metal borates (Fe_3BO_5 and NiBO) were successfully synthesized by a facile sol-gel method, which exhibit significantly higher Na-ion insertion activity and reversible capacity than transition metal oxides (Fe_3O_4 and NiO). Furthermore, the conversion mechanism of the transition metal borates was also studied. The conversion reaction can be completely realized for transition metal borates during the sodiation/desodiation, while only a part of transition metal oxide can be transformed under the same condition. It's revealed by first-principle calculations that it requires much lower energy when Na-ion insert into borates compared with oxides. At last, carbon coated borates were designed and triumphantly fabricated, which display much enhanced rate capability and excellent cycling stability. This study provides a class of new promising conversion-type anodes for NIBs and comprehensive study of their structure and properties.

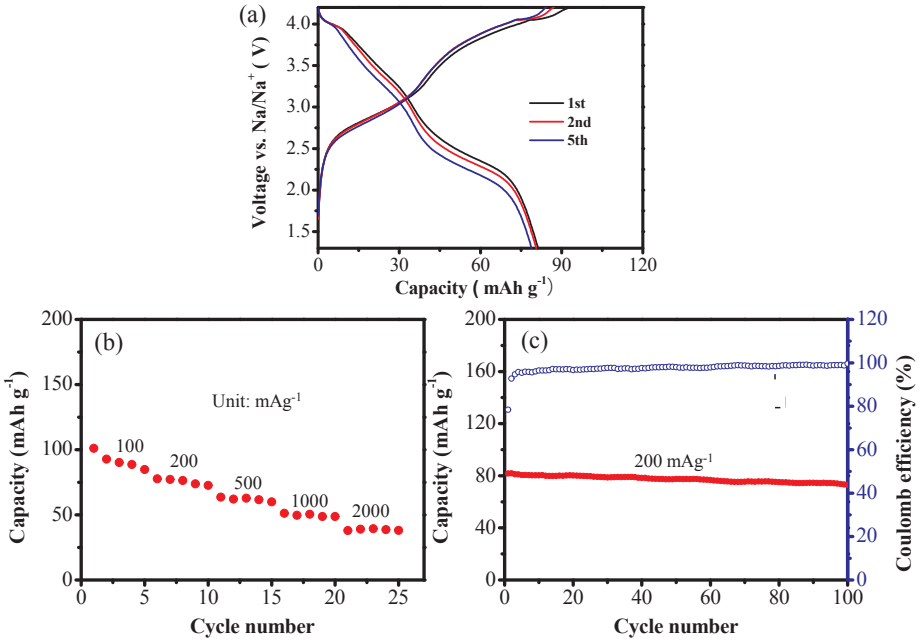

Fig. 7. Galvanostatic discharge and charge profiles for the 1st, 2nd and 5th cycles of (c) Fe_3BO_5/$Na_2V_3(PO_4)_2F_3$ full cell at a current density of 200 mAg^{-1}. (b) Rate capability of Fe_3BO_5/$Na_2V_3(PO_4)_2F_3$ full cell at the current density range from 100 to 2000 mAg^{-1}. (c) Cycling performance and Coulombic efficiency of Fe_3BO_5/$Na_2V_3(PO_4)_2F_3$ full cell at a current density of 200 mAg^{-1}.

Acknowledgements

National Natural Science Foundation of China (NSFC 51874099 and 51502038) and National Science Foundation of Fujian Province (2018J06012 and 2016J01011) provide the financial support of this study. Z. Hong and G. Xu would like to thank the support from Fujian Provincial College Funds for Distinguished Young Scientists of year 2017 and 2015, respectively. We also thank the Undergraduate Training Programs for Innovation and Entrepreneurship of Fujian University (S201910394012, 201810394009).

Appendix A. Supplementary data

Computational method, additional XRD, SEM images and CV curves are shown in the supporting information.

Supplementary data to this article can be found online at https://doi.org/10.1016/j.cej.2019.121998.

References

[1] Z. Yang, J. Zhang, M.C.W. Kintner-Meyer, X. Lu, D. Choi, J.P. Lemmon, J. Liu, Electrochemical energy storage for green grid, Chem. Rev. 111 (2011) 3577–3613.
[2] R. Schmuch, R. Wagner, G. Hörpel, T. Placke, M. Winter, Performance and cost of materials for lithium-based rechargeable automotive batteries, Nat. Energy 3 (2018) 267–278.
[3] B. Yin, X. Cao, A. Pan, Z. Luo, S. Dinesh, J. Lin, Y. Tang, S. Liang, G. Cao, Encapsulation of CoSx Nanocrystals into N/S Co-Doped Honeycomb-Like 3D Porous Carbon for High-Performance Lithium Storage, Adv. Sci. 5 (2018) 1800829.
[4] P.K. Nayak, L. Yang, W. Brehm, P. Adelhelm, From lithium-ion to sodium-ion batteries: advantages, challenges, and surprises, Angew. Chem. Int. Ed. 57 (2018) 102–120.
[5] A. Eftekhari, D.-W. Kim, Sodium-ion batteries: new opportunities beyond energy storage by lithium, J. Power Sources 395 (2018) 336–348.
[6] D. Kundu, E. Talaie, V. Duffort, L.F. Nazar, The emerging chemistry of sodium ion batteries for electrochemical energy storage, Angew. Chem. Int. Ed. 54 (2015) 3431–3448.
[7] G. Parzych, D. Mikhailova, S. Oswald, J.R. Eckert, H. Ehrenberg, Study of the conversion reaction mechanism for copper borate as electrode material in lithium-ion batteries, J. Electrochem. Soc. 158 (2011) A898.
[8] H. Kang, Y. Liu, K. Cao, Y. Zhao, L. Jiao, Y. Wang, H. Yuan, Update on anode materials for Na-ion batteries, J. Mater. Chem. A 3 (2015) 17899–17913.
[9] L.P. Wang, L. Yu, X. Wang, M. Srinivasan, Z.J. Xu, Recent developments in electrode materials for sodium-ion batteries, J. Mater. Chem. A 3 (2015) 9353–9378.
[10] Y. Liang, W.H. Lai, Z. Miao, S.L. Chou, Nanocomposite materials for the sodium-ion battery: a review, Small 14 (2018) 1703671.
[11] L. Li, Y. Zheng, S. Zhang, J. Yang, Z. Shao, Z. Guo, Recent progress on sodium ion batteries: potential high-performance anodes, Energy Environ. Sci. 11 (2018) 2301.
[12] Z. Hong, Y. Zhen, Y. Ruan, M. Kang, K. Zhou, J.M. Zhang, Z. Huang, M. Wei, rational design and general synthesis of s-doped hard carbon with tunable doping sites toward excellent na-ion storage performance, Adv. Mater. 30 (2018) 1802035.
[13] Y. Mei, Y. Huang, X. Hu, Nanostructured Ti-based anode materials for Na-ion batteries, J. Mater. Chem. A 4 (2016) 12001–12013.
[14] Z. Hong, K. Zhou, J. Zhang, Z. Huang, M. Wei, Facile synthesis of rutile TiO_2 mesocrystals with enhanced sodium storage properties, J. Mater. Chem. A 3 (2015) 17412–17416.
[15] S. Peng, X. Han, L. Li, Z. Zhu, F. Cheng, M. Srinivansan, S. Adams, S. Ramakrishna, Unique cobalt sulfide/reduced graphene oxide composite as an anode for sodium-ion batteries with superior rate capability and long cycling stability, Small 12 (2016) 1359–1368.
[16] D. Zhang, W. Sun, Y. Zhang, Y. Dou, Y. Jiang, S.X. Dou, Engineering hierarchical hollow nickel sulfide spheres for high-performance sodium storage, Adv. Funct. Mater. 26 (2016) 7479–7485.
[17] Y. Wang, Y. Zhang, J. Shi, A. Pan, F. Jiang, S. Liang, G. Cao, S-doped porous carbon confined SnS nanospheres with enhanced electrochemical performance for sodium-ion batteries, J. Mater. Chem. A 6 (2018) 18286–18292.
[18] M. Lao, Y. Zhang, W. Luo, Q. Yan, W. Sun, S.X. Dou, Alloy-based anode materials toward advanced sodium-ion batteries, Adv. Mater. 29 (2017) 1700622.
[19] C. Wang, L. Wang, F. Li, F. Cheng, J. Chen, Bulk bismuth as a high-capacity and ultralong cycle-life anode for sodium-ion batteries by coupling with glyme-based electrolytes, Adv. Mater. 29 (2017) 1702212.
[20] Y. Zhao, L.P. Wang, M.T. Sougrati, Z. Feng, Y. Leconte, A. Fisher, M. Srinivasan, Z. Xu, A review on design strategies for carbon based metal oxides and sulfides nanocomposites for high performance Li and Na ion battery anodes, Adv. Energy Mater. 7 (2017) 1601424.
[21] K. Chayambuka, G. Mulder, D.L. Danilov, P.H.L. Notten, Sodium-ion battery materials and electrochemical properties reviewed, Adv. Energy Mater. 8 (2018) 1800079.
[22] J. Cabana, L. Monconduit, D. Larcher, M.R. Palacin, Beyond intercalation-based Li-ion batteries: the state of the art and challenges of electrode materials reacting through conversion reactions, Adv. Mater. 22 (2010) E170–192.
[23] H.-H. Li, Z.-Y. Li, X.-L. Wu, L.-L. Zhang, C.-Y. Fan, H.-F. Wang, X.-Y. Li, K. Wang, H.-Z. Sun, J.-P. Zhang, Shale-like Co_3O_4 for high performance lithium/sodium ion batteries, J. Mater. Chem. A 4 (2016) 8242–8248.
[24] F. Zou, Y.M. Chen, K. Liu, Z. Yu, W. Liang, S.M. Bhaway, M. Gao, Y. Zhu, Metal organic frameworks derived hierarchical hollow NiO/Ni/Graphene composites for lithium and sodium storage, ACS Nano 10 (2016) 377–386.
[25] G. Gao, H.B. Wu, X.W.D. Lou, Citrate-assisted growth of $NiCo_2O_4$ nanosheets on reduced graphene oxide for highly reversible lithium storage, Adv. Energy Mater. 4 (2014) 1400422.
[26] Z. Jian, P. Liu, F. Li, M. Chen, H. Zhou, Monodispersed hierarchical Co_3O_4 spheres intertwined with carbon nanotubes for use as anode materials in sodium-ion batteries, J. Mater. Chem. A 2 (2014) 13805.
[27] Z. Hong, K. Zhou, Z. Huang, M. Wei, Iso-oriented anatase TiO_2 mesocages as a high performance anode material for sodium-ion storage, Sci. Rep. 5 (2015) 11960.
[28] Z. Hong, M. Kang, X. Chen, K. Zhou, Z. Huang, M. Wei, Synthesis of mesoporous Co^{2+}-Doped TiO_2 nanodisks derived from metal organic frameworks with improved sodium storage performance, ACS Appl. Mater. Interfaces 9 (2017) 32071–32079.
[29] Y. Idota, T. Kubota, A. Matsufuji, Y. Maekawa, T. Miyasaka, Tin-based amorphous oxide: a high-capacity lithium-ion-storage material, Science 276 (1997) 1395.
[30] J.L.C. Rowsell, J. Gaubicher, L.F. Nazar, A new class of materials for lithium-ion

batteries: iron(III) borates, J. Power Sources 97–98 (2001) 254–257.
[31] J.L.C. Rowsell, L.F. Nazar, Synthesis, structure, and solid-state electrochemical properties of Cr_3BO_6: a new chromium(iii) borate with the norbergite structure, J. Mater. Chem. 11 (2001) 3228–3233.
[32] F. Strauss, G. Rousse, D. Batuk, M. Tang, E. Salager, G. Drazic, R. Dominko, J.M. Tarascon, Electrochemical behavior of $Bi_4B_2O_9$ towards lithium-reversible conversion reactions without nanosizing, Phys. Chem. Chem. Phys. 20 (2018) 2330–2338.
[33] A. Débart, B. Revel, L. Dupont, L. Montagne, J.B. Leriche, M. Touboul, J.M. Tarascon, Study of the Reactivity Mechanism of $M_3B_2O_6$ (with M = Co, Ni, and Cu) toward lithium, Chem. Mater. 15 (2003) 3683–3691.
[34] V. Singh, V. Srinivas, S. Ram, A. Ghoshray, B. Bandyopadhyay, Evidence For Anti-ferromagnetism In NiO/$Ni_3B_2O_6$ Nanocomposites, AIP Conf. Proc. 1003 (2008) 49–51.
[35] J. Li, L. Zhang, Y. Gu, Q. Qian, J. Wang, G. Zhao, X. Pan, High-yield synthesis of boron nitride nanotubes by annealing Fe_3BO_6, Chem. Lett. 40 (2011) 540–541.
[36] J. Tian, B. Wang, F. Zhao, X. Ma, Y. Liu, H.K. Liu, Z. Huang, Highly active Fe_3BO_6 as an anode material for sodium-ion batteries, Chem. Commun. 53 (2017) 4698–4701.
[37] X.X. Shi, X.J. Liu, L.J. Yuan, The electrochemical property of cobalt borate as a novel anode material for lithium-ion battery, Adv. Mater. Res. 236 (2011) 876–879.
[38] S. Li, L. Xu, Y. Zhai, H. Yu, Co-pyrolysis synthesis of Fe_3BO_6 nanorods as high performance anodes for lithium-ion batteries, RSC Adv. 4 (2014) 8245.
[39] P. Liang, L. Du, X. Wang, Z.-H. Liu, Preparation of $Ni_3B_2O_6$ nanosheet-based flowerlike architecture by a precursor method and its electrochemical properties in lithium-ion battery, Solid State Sci. 37 (2014) 131–135.
[40] A. Ibarra Palos, M. Morcrette, P. Strobel, Reversible lithium intercalation in amorphous iron borate, J. Solid State Electrochem. 6 (2002) 134–138.
[41] S. Wang, X.B. Zhang, N-Doped C@$Zn_3B_2O_6$ as a low cost and environmentally friendly anode material for na-ion batteries: high performance and new reaction mechanism, Adv. Mater. 31 (2018) 1805432.
[42] J. He, L. Luo, Y. Chen, A. Manthiram, Yolk-Shelled C@Fe_3O_4 nanoboxes as efficient sulfur hosts for high-performance lithium-sulfur batteries, Adv. Mater. 29 (2017) 1702707.
[43] P.R. Kumar, Y.H. Jung, K.K. Bharathi, C.H. Lim, D.K. Kim, High capacity and low cost spinel Fe_3O_4 for the Na-ion battery negative electrode materials, Electrochim. Acta 146 (2014) 503–510.
[44] Y. Fu, Q. Wei, X. Wang, G. Zhang, H. Shu, X. Yang, A.C. Tavares, S. Sun, A facile synthesis of Fe_3O_4 nanoparticles/graphene for high-performance lithium/sodium-ion batteries, RSC Adv. 6 (2016) 16624–16633.
[45] Z.-G. Wu, Y.-J. Zhong, J. Liu, J.-H. Wu, X.-D. Guo, B.-H. Zhong, Z.-Y. Zhang, Subunits controlled synthesis of α-Fe_2O_3 multi-shelled core–shell microspheres and their effects on lithium/sodium ion battery performances, J. Mater. Chem. A 3 (2015) 10092–10099.
[46] S. Zhang, W. Li, B. Tan, S. Chou, Z. Li, S. Dou, One-pot synthesis of ultra-small magnetite nanoparticles on the surface of reduced graphene oxide nanosheets as anodes for sodium-ion batteries, J. Mater. Chem. A 3 (2015) 4793–4798.
[47] J. Yang Lee, Y. Xiao, Z. Liu, Amorphous $Sn_2P_2O_7$, $Sn_2B_2O_5$ and Sn_2BPO_6 anodes for lithium ion batteries, Solid State Ionics 133 (2000) 25–35.
[48] E.M. Abou Hussein, N.A. El-Alaily, Study on the effect of gamma radiation on some spectroscopic and electrical properties of lithium borate glasses, J. Inorg. Organomet. P 28 (2018) 1214–1225.
[49] B.R. Strohmeier, Surface characterization of aluminum foil annealed in the presence of ammonium fluoborate, Appl. Surf. Sci. 40 (1989) 249–263.
[50] L. Liu, L. Hong, Ceria-supported nickel borate as a sulfur-tolerant catalyst for autothermal reforming of a proxy jet fuel, Catalysis Today 263 (2016) 52–60.
[51] X. Shi, C. Chang, J. Xiang, Y. Xiao, L. Yuan, J. Sun, Synthesis of nanospherical Fe_3BO_6 anode material for lithium-ion battery by the rheological phase reaction method, J. Solid State Chem. 181 (2008) 2231–2236.
[52] G. Xu, Q. Wu, Z. Chen, Z. Huang, R. Wu, Y.P. Feng, Disorder and surface effects on work function of Ni-Pt metal gates, Phys. Rev. B 78 (2008) 115420.
[53] H. Zhang, Y. Tang, J. Shen, X. Xin, L. Cui, L. Chen, C. Ouyang, S. Shi, L. Chen, Antisite defects and Mg doping in $LiFePO_4$: a first-principles investigation, Appl. Phys. A 104 (2011) 529–537.
[54] Y. Cai, X. Cao, Z. Luo, G. Fang, F. Liu, J. Zhou, A. Pan, S. Liang, Caging $Na_3V_2(PO_4)_2F_3$ microcubes in cross-linked graphene enabling ultrafast sodium storage and long-term cycling, Adv. Sci. 5 (2018) 1800680.